

Distinguishing nonstandard scalar and fermionic charged particles at a future e^+e^- collider

Anjan Kumar Barik^{✉,*}, Rafiqul Rahaman^{✉,†} and Santosh Kumar Rai^{✉,‡}

*Regional Centre for Accelerator-based Particle Physics, Harish-Chandra Research Institute,
A CI of Homi Bhabha National Institute, Chhatnag Road, Jhansi, Prayagraj 211019, India*

 (Received 15 July 2022; accepted 11 January 2023; published 2 February 2023)

We investigate the possibility to identify the intrinsic spin of exotic charged particles at a future e^+e^- collider in the $l^\pm + 2j + \cancel{E}_T$ final state. We choose the inert doublet model (IDM) and minimal supersymmetric standard model (MSSM) as examples for the new physics models with scalar and fermionic exotic charged particles, respectively. The signal arises when these exotic charged particles are pair produced and then decay to a W^\pm boson and the lightest neutral stable particle in the new physics model. We choose four benchmarks for the mass parameters which give significant deviation from the dominant standard model (SM) W^+W^- background. We find that an asymmetry in the cosine of the scattering angle ($\cos\theta$) of one of the W bosons reconstructed from jj pair as well as the charged lepton have the potential to identify the MSSM and IDM signal over SM with longitudinally polarized initial beams. A more robust distinction is seen in the shape of the azimuthal angle distribution of the W boson and charged lepton, which can identify and distinguish the IDM signal from MSSM further if the initial beams are transversely polarized.

DOI: [10.1103/PhysRevD.107.035002](https://doi.org/10.1103/PhysRevD.107.035002)

I. INTRODUCTION

The standard model (SM) of particle physics has been a great success in explaining most of the phenomena in nature. Despite its huge success, phenomena such as the existence of nonzero neutrino mass and their oscillation, the presence of dark matter (DM) in the Universe, the obvious matter-antimatter asymmetry vis-a-vis baryogenesis, stability of the electroweak scale, or the gauge hierarchy problem, etc., require one to think of physics beyond the SM (BSM). A plethora of candidate BSM models exist in the literature to address such nonstandard phenomena. These BSM models are being probed at the current Large Hadron Collider (LHC), and strategies are being set up to probe them with more precision at future colliders such as High Luminosity LHC (HL-LHC) [1], High Energy LHC (HE-LHC) [2], International Linear Collider (ILC) [3–6], Large Hadron electron Collider (LHeC) [7], Future Circular Collider (FCC) [8,9], etc. A very obvious and well-known aspect of having so many

different BSM theories is the so-called inverse problem, where different models lead to overlapping outputs in the signal space, and it becomes challenging to map it to any given BSM scenario. Therefore, the chances of observing that rare event of new physics, which has proven to be so elusive at LHC, may have too many BSM candidates to claim as their own, since similar collider signatures can arise from different BSM models. Not much attention has been paid to identifying the type of BSM models by looking at collider signatures [10–12]. We try to fill up a gap in this direction by showing through this work how to distinguish two types of BSM models by looking at similar signatures at colliders based on the spins of exotic particles. Typically, one expects to be able to identify spin [10,13–15] of a mediator by looking at the angular distribution in a $2 \rightarrow 2$ scattering process where the final state particles are SM fields. We consider a more common configuration which appears in models that have a DM candidate that would escape detection. The lightest neutral stable particles (LNSP) in these models can play a good dark matter candidate. These models also predict charged particles that decay to LNSP. These BSM charged particles together with the LNSP can have different spins (0, 1/2, and 1) in different models. Understanding the spin nature of dark matter (LNSP) experimentally is of particular importance not only for particle physics, but also for astrophysics and cosmology.

In this article, we investigate the possibility of identifying the spin of BSM charged particles or the candidate dark

*anjanbarik@hri.res.in

†rafiqulrahaman@hri.res.in

‡skrai@hri.res.in

Published by the American Physical Society under the terms of the Creative Commons Attribution 4.0 International license. Further distribution of this work must maintain attribution to the author(s) and the published article's title, journal citation, and DOI. Funded by SCOAP³.

matter through the collider signature of pair production of BSM charged particles followed by their decay to LNSP and W^\pm boson. It is not easy to do such precision measurements at the LHC, as it is overwhelmed by the huge QCD background. A future e^+e^- collider or ILC, on the other hand, offers a great possibility in this direction for having a clean signature with a very low background and extra handles such as beam polarization (longitudinal and transverse) [16]. We choose two well-motivated models as examples, the inert doublet model (IDM) [17,18] and the minimal supersymmetric SM (MSSM) [19,20], having potential dark matter candidates of type scalar (spin-0) and fermion (spin-1/2), respectively to study the collider signature of the process

$$e^+e^- \rightarrow C^+C^- \rightarrow C^0C^0W^+W^- \quad (1)$$

In IDM, the C^+ and C^0 are Z_2 -odd charged Higgs (H^\pm) and neutral Higgs (H^0), while for MSSM, they are the chargino ($\tilde{\chi}^\pm$) and neutralino ($\tilde{\chi}^0$), respectively. Note that the charged and neutral scalars (fermions) can appear in several BSM setups involving Z_2 -odd parity, and, therefore, this analysis will be applicable in all such scenarios. We use the potential of beam polarization (both longitudinal and transverse) of an e^+e^- collider to discriminate between the two models by looking at various angular distributions in the $l^\pm jj + \cancel{E}_T$ final states.

The rest of the article is organized as follows. In the next section (Sec. II), we briefly review IDM and MSSM, along with benchmark points for the new physics parameters such as masses and couplings. In Sec. III, we discuss the signal and corresponding SM background, followed by the analysis setup. In Sec. IV A, we study various kinematic and angular distributions with longitudinal beam polarization and perform an analysis with a simple cut and count on the variables. We then try to determine the spin of the exotic charged particles and their partner with the help of transverse beam polarization in Sec. IV B. Finally, we conclude in Sec. V.

II. REPRESENTATIVE MODEL

We choose two well-motivated models, IDM and MSSM, as examples of having exotic charged particles and their neutral partner (potential dark matter) of scalar type and fermionic type, respectively. These models are briefly described below to self-contain this article.

A. The inert doublet model

In the IDM [21], the scalar sector of the SM is modified with one additional scalar doublet Φ , which is odd ($\Phi \rightarrow -\Phi$) under a new discrete Z_2 symmetry (parity). The SM particles together with the SM Higgs doublet (H) are even under this Z_2 symmetry. The two scalar doublets which transform under $SU(2)_L$ can be written as

$$H = \begin{pmatrix} G^+ \\ \frac{1}{\sqrt{2}}(v + h + iG^0) \end{pmatrix}, \quad \Phi = \begin{pmatrix} H^+ \\ \frac{1}{\sqrt{2}}(H^0 + iA^0) \end{pmatrix}, \quad (2)$$

where $v = \sqrt{2}\langle 0|H|0\rangle \approx 246$ GeV is the vacuum expectation value of the neutral component of H . The h state corresponds to the physical SM-like Higgs boson, whereas G^0 and G^\pm are the Goldstone bosons. The ‘‘inert’’ sector consists of a neutral CP -even scalar H^0 , a pseudoscalar A^0 , and a pair of charged scalars H^\pm . The neutral inert Higgs (H^0) and its charged partner (H^\pm) play the role of dark matter and the new exotic charged particle, respectively.

The scalar potential of the model is given by

$$V = \mu_1^2|H|^2 + \mu_2^2|\Phi|^2 + \lambda_1|H|^4 + \lambda_2|\Phi|^4 + \lambda_3|H|^2|\Phi|^2 + \lambda_4|H^\dagger\Phi|^2 + \frac{\lambda_5}{2}[(H^\dagger\Phi)^2 + \text{H.c.}] \quad (3)$$

The masses and interactions of the scalar sector are governed by the scalar-potential parameters

$$\{\lambda_1, \lambda_2, \lambda_3, \lambda_4, \lambda_5, \mu_2\}, \quad (4)$$

where μ_1^2 is eliminated by $M_h^2 = -2\mu_1^2 = 2\lambda_1v^2$ which is obtained by minimizing the scalar potential after electro-weak symmetry breaking. The IDM parameter space can be expressed in terms of the physically more intuitive set

$$\{M_h, M_{H^0}, M_{A^0}, M_{H^\pm}, \lambda_L, \lambda_S\}, \quad (5)$$

where the Higgs and inert scalar masses are given by

$$M_h^2 = \mu_1^2 + 3\lambda_1v^2, \quad (6)$$

$$M_{H^0}^2 = \mu_2^2 + \lambda_Lv^2, \quad (7)$$

$$M_{A^0}^2 = \mu_2^2 + \lambda_Sv^2, \quad (8)$$

$$M_{H^\pm}^2 = \mu_2^2 + \frac{1}{2}\lambda_3v^2, \quad (9)$$

and the couplings λ_L and λ_S are defined, respectively, as

$$\lambda_L = \frac{1}{2}(\lambda_3 + \lambda_4 + \lambda_5) \\ \lambda_S = \frac{1}{2}(\lambda_3 + \lambda_4 - \lambda_5). \quad (10)$$

The interaction Lagrangian in our signal comprising the production and decay vertices of H^\pm originating from gauge interactions can be written as

$$\begin{aligned} \mathcal{L} = & i[g_Z(1/2 - s_W^2)Z^\mu + eA^\mu][(\partial_\mu H_S^+)H_S^- - (\partial_\mu H_S^-)H_S^+] \\ & + (g/2)[-(\partial^\mu H_S^+)H_S^0 W_\mu^- + (\partial^\mu H_S^0)H_S^+ W_\mu^- + \text{H.c.}] \end{aligned} \quad (11)$$

Here, $e = \sqrt{4\pi\alpha}$ with α being fine structure constant, g as the $SU(2)_L$ gauge couplings, $g_z = e/(s_W c_W)$, $s_W = \sin \theta_W$, and $c_W = \cos \theta_W$ with θ_W being the Weinberg angle.

B. Minimal supersymmetric SM

We briefly discuss the basic setup of the model and the relevant spectrum used in our analysis. The MSSM [22] is the supersymmetric extension of SM where for every SM fermion (boson) there is a boson (fermion) superpartner. The MSSM has two Higgs doublet superfields with

$$\begin{aligned} \mathcal{L} \supset & i\tilde{H}_{1i}\sigma^\mu\Delta_{\mu ij}\tilde{H}_{1j} + i\tilde{H}_{2i}\sigma^\mu\Delta_{\mu ij}\tilde{H}_{2j} + \mu\epsilon_{ab}\tilde{H}_{1a}\tilde{H}_{2b} + i\tilde{B}\sigma^\mu\partial_\mu\tilde{B} + i\lambda_i\sigma^\mu\Delta_{\mu ij}\tilde{\lambda}_j \\ & - \frac{1}{2}M_1\tilde{B}\tilde{B} - \frac{1}{2}M_2\lambda_i\lambda_i - \sqrt{2}g_2\tilde{H}_{1i}\lambda_a\frac{\sigma_{ij}^a}{2}H_{1j} - \sqrt{2}g_2\tilde{H}_{2i}\lambda_a\frac{\sigma_{ij}^a}{2}H_{2j} \\ & - \sqrt{2}g_1\frac{\hat{Y}_i}{2}\tilde{B}\tilde{H}_{1i}H_{1i} - \sqrt{2}g_1\frac{\hat{Y}_i}{2}\tilde{B}\tilde{H}_{2i}H_{2i} + \text{H.c.}, \end{aligned} \quad (12)$$

where

$$\Delta_{ij}^\mu = \delta_{ij}\partial^\mu + ig_1\frac{\hat{Y}_i}{2}\delta_{ij}B_\mu + ig_2W^{\mu a}T_{ij}^a.$$

Here \hat{Y} and T^a , respectively, represent hypercharge and $SU(2)$ generators in the respective representation of the field over which these operator act and

$$\tilde{H}_1 = \begin{pmatrix} \tilde{h}_1^1 \\ \tilde{h}_1^2 \end{pmatrix}, \quad \tilde{H}_2 = \begin{pmatrix} \tilde{h}_2^1 \\ \tilde{h}_2^2 \end{pmatrix}, \quad \tilde{B}, \quad \lambda_s = (\lambda_1, \lambda_2, \lambda_3)$$

are the fermionic superpartners of two Higgs fields H_1 and H_2 and the superpartners of $U(1)$ and $SU(2)$ gauge fields, respectively. Here, the neutral sector of SUSY fermionic partners of the SM bosons consist of neutral Weyl fermions (\tilde{B} , λ_3 , \tilde{h}_1^1 , \tilde{h}_2^2), and the charge sector comprises of (\tilde{h}_2^1 , \tilde{h}_1^2 , $\lambda^+ \equiv \frac{\lambda_1 - i\lambda_2}{\sqrt{2}}$, $\lambda^{-c} \equiv \frac{\lambda_1 + i\lambda_2}{\sqrt{2}}$, superscript c being the charge conjugation operator) two-component Weyl fermions.

Spontaneous symmetry breaking is realized through the vacuum expectation value (VEV) for the two Higgs fields H_1 and H_2 with VEV $\langle \frac{v_1}{\sqrt{2}} \rangle$ and $\langle \frac{v_2}{\sqrt{2}} \rangle$, respectively. Here, we define electroweak VEV $v = \sqrt{v_1^2 + v_2^2}$ with $\tan \beta = \frac{v_2}{v_1}$.

After electroweak symmetry breaking, the mass term for the Higgsino and electroweakino charged sector becomes

opposite hypercharge (needed to cancel the resulting gauge anomaly). Supersymmetry (SUSY) cannot be an exact symmetry, as it would lead to similar mass for the superpartners of the SM particles. SUSY is softly broken and in MSSM through explicit mass terms for the superpartners of the SM particles. The Lagrangian in MSSM has a discrete global symmetry called R parity (R_P), defined as $(-1)^{3B-L+2S}$, whereas all SM particles are even under R_P while their superpartners have $R_P = -1$. This makes the lightest SUSY particle (LSP) stable and is considered as a DM candidate. For our analysis, we consider the LSP as a composition of the Higgsino and gaugino states of MSSM. The Lagrangian containing only Higgsinos and gauginos is given by

$$\begin{aligned} \mathcal{L}_{\text{Mass}}^c = & -\frac{g_2}{\sqrt{2}}(v_1\lambda^+\tilde{h}_1^2 + v_2\lambda^-\tilde{h}_2^1 + \text{H.c.}) \\ & - (M_2\lambda^+\lambda^- + \mu\tilde{h}_1^2\tilde{h}_2^1 + \text{H.c.}). \end{aligned} \quad (13)$$

In the basis

$$\psi^+ = \begin{pmatrix} \lambda^+ \\ \tilde{h}_2^1 \end{pmatrix}$$

and

$$\psi^- = \begin{pmatrix} \lambda^- \\ \tilde{h}_1^2 \end{pmatrix},$$

the above Lagrangian can be written as

$$-\mathcal{L}_{\text{Mass}}^c = (\psi^-)^T \begin{pmatrix} M_2 & \sqrt{2}M_W \sin \beta \\ \sqrt{2}M_W \cos \beta & \mu \end{pmatrix} \psi^+. \quad (14)$$

As the mass matrix is not symmetric, it has to be diagonalized by a biunitary transformation:

$$M_c^D = \mathcal{U}^* \begin{pmatrix} M_2 & \sqrt{2}M_W \sin \beta \\ \sqrt{2}M_W \cos \beta & \mu \end{pmatrix} \mathcal{V}^{-1}, \quad (15)$$

where M_c^D is a diagonal matrix with real positive eigenvalues. Weyl fermion eigenstates will be $\chi_k^+ = \mathcal{V}_{km}\psi_m^+$ and

$\chi_k^- = \mathcal{U}_{km}\psi_m^-$, which can be written as a four-component chargino field. The mass for the charginos can be written as

$$-\mathcal{L}_{\text{Mass}}^c = \tilde{M}_1 \overline{\tilde{\chi}_1^+} \tilde{\chi}_1^+ + \tilde{M}_2 \overline{\tilde{\chi}_2^+} \tilde{\chi}_2^+, \quad (16)$$

where

$$\tilde{\chi}_1^+ \equiv \begin{pmatrix} \tilde{\chi}_1^+ \\ \overline{\tilde{\chi}_1^+}^T \end{pmatrix}$$

and

$$\tilde{\chi}_2^+ \equiv \begin{pmatrix} \tilde{\chi}_2^+ \\ \overline{\tilde{\chi}_2^+}^T \end{pmatrix}$$

are chargino fields. The Lagrangian in the neutral electro-weakino sector can be written as

$$\begin{aligned} \mathcal{L}_{\text{Mass}}^n = & -\frac{g_2}{2} \lambda_3 (v_1 \tilde{h}_1^1 - v_2 \tilde{h}_2^2) + \frac{g_1}{2} \tilde{B} (v_1 \tilde{h}_1^1 - v_2 \tilde{h}_2^2) \\ & + \mu \tilde{h}_1^1 \tilde{h}_2^2 - \frac{1}{2} M_2 \lambda_3 \lambda_3 - \frac{1}{2} M_1 \tilde{B} \tilde{B} + \text{H.c.} \end{aligned} \quad (17)$$

The mass matrix, in the basis of $\psi^0 = (\tilde{B}, \lambda_3, \tilde{h}_1^1, \tilde{h}_2^2)$ is given by

$$\mathcal{M}^n = \begin{pmatrix} M_1 & 0 & -M_z c_\beta s_W & M_z s_\beta s_W \\ 0 & M_2 & M_z c_\beta c_W & -M_z s_\beta c_W \\ -M_z c_\beta s_W & M_z c_\beta c_W & 0 & -\mu \\ M_z s_\beta s_W & -M_z s_\beta c_W & -\mu & 0 \end{pmatrix}. \quad (18)$$

This matrix can be diagonalized by a unitary matrix Z . The physical mass eigenstates and the mass diagonalization matrix are given by $\chi_l^0 = Z_{ln} \psi_n^0$ and $Z^* \mathcal{M} Z^{-1} = M_D^n$, respectively. In the four-component notation, the mass term in the Lagrangian for neutralinos can be written as

$$\mathcal{L}_{\text{Mass}}^n = -\frac{1}{2} \sum_l \tilde{M}_l^n \overline{\tilde{\chi}_l^0} \tilde{\chi}_l^0, \text{ where}$$

$$\tilde{\chi}_l^0 = \begin{pmatrix} \chi_l^0 \\ \overline{\tilde{\chi}_l^0}^T \end{pmatrix}$$

are the four Majorana neutralino fields. The lowest mass eigenstate of four neutralinos will be the LSP and represents the DM candidate.

The masses and vertices relevant for our analysis except the gauge couplings depend only on four parameters, which are the soft breaking gaugino mass parameters (M_1 and M_2), the Higgsino mass parameter (μ), and the ratio of the VEV of the Higgs doublets ($\tan\beta$). The lightest chargino mass eigenstate coupling to the Z boson depends on the chargino mixing matrix elements \mathcal{V}_{11} and \mathcal{U}_{11} [23]. For simplicity, we keep these matrix elements fixed for all our

benchmark points which can be obtained by varying the input parameters M_2 , μ , and $\tan\beta$ of the model.

C. Benchmark selection

We choose four benchmark points (BPs), in our analysis, for the masses of exotic charged particles (C^\pm) and their neutral partner (C^0) in both IDM and MSSM. The benchmark points are listed in Table I. The BPs are chosen in such a way that $\Delta M = M^+ - M^0$ ($M^+ = M_{C^+}$, $M^0 = M_{C^0}$) remain fixed for two BPs with different M^+ and M^0 (BP1 and BP3); two BPs have the same M^+ but with a different ΔM (BP2 and BP3); three BPs satisfy these criteria. We choose one more BP which has a different M^+ and ΔM compared to the other three (BP4).

The mass parameters are kept the same in both models in order to have similar kinematic behavior. Through all four BPs, the mass difference between charged odd particle with the respective DM particle is kept higher than the mass of the W boson, so that both the W boson and DM particle can be produced on shell from their parent charged dark sector particle. In IDM, there are two coupling parameters, λ_L and λ_S , which can affect the SM Higgs signal in our study. The value of λ_L is kept very small so that the second neutral CP -even Higgs mass (m_{H_0}), which is the DM, is nearly equal to μ_2 [see Eq. (7)]. The value of λ_S is chosen such that $m_{A_0} - m_{H^\pm} = 1$ GeV. These two choices help us in evading the bound on Higgs invisible decay as well as electroweak precision observables. For all four BPs of MSSM, we have kept the chargino mixing matrices to be the same with $\mathcal{V}_{11} \equiv \cos\theta_R = 0.9725$ and $\mathcal{U}_{11} \equiv \cos\theta_L = 0.9168$. We do not focus on whether the benchmarks satisfy the requirements of dark matter relic density. However, we keep BP1 as a reference point which does satisfy dark matter constraints [12]. Apart from the dark matter constraint, there are other constraints that are considered while choosing the BPs, which we discuss below.

I. Constraints

a. Vacuum stability and unitarity

In IDM, the scalar potential must be bounded from below. The conditions on various quartic couplings to satisfy this constraint are given by [24]

TABLE I. Benchmark points for the MSSM and IDM.

Benchmark	Masses
BP1	$M_\pm = 160$ GeV, $M_0 = 60$ GeV
BP2	$M_\pm = 220$ GeV, $M_0 = 100$ GeV
BP3	$M_\pm = 220$ GeV, $M_0 = 120$ GeV
BP4	$M_\pm = 300$ GeV, $M_0 = 10$ GeV

$$\begin{aligned} \lambda_1 > 0, \quad \lambda_2 > 0, \quad 2\sqrt{\lambda_1\lambda_2} + \lambda_3 > 0, \\ 2\sqrt{\lambda_1\lambda_2} + \lambda_3 + \lambda_4 - |\lambda_5| > 0. \end{aligned} \quad (19)$$

We have checked that all our four BPs for IDM satisfy the above conditions. In addition, we have also checked that the BPs satisfy unitarity bounds [24].

b. Electroweak precision observables

The BSM particles affect the electroweak (EW) observables via oblique correction, and these corrections are parametrized by three observables S , T , and U as electroweak precision observables (EWPOs). The contribution to EWPOs (S and T) from IDM are given by [24]

$$\begin{aligned} S = \frac{1}{72\pi(x_2^2 - x_1^2)^3} \\ \times [x_2^6 f_a(x_2) - x_1^6 f_a(x_1) + 9x_2^2 x_1^2 (x_2^2 f_b(x_2) - x_1^2 f_b(x_1))], \end{aligned} \quad (20)$$

where $x_1 = \frac{M_{H^0}}{M_{H^\pm}}$, $x_2 = \frac{M_A}{M_{H^\pm}}$, $f_a(x) = -5 + 12 \log(x)$, $f_b(x) = 3 - 4 \log(x)$, and

$$\begin{aligned} T = \frac{1}{32\pi^2 \alpha v^2} \\ \times [f_c(M_{H^+}^2, M_A^2) - f_c(M_A^2, M_{H^0}^2) + f_c(M_{H^+}^2, M_{H^0}^2)], \end{aligned} \quad (21)$$

where

$$f_c(x, y) = \begin{cases} \frac{x+y}{2} - \frac{xy \log(\frac{x}{y})}{x-y}, & x \neq y \\ 0, & x = y. \end{cases}$$

The experimental values of S and T with $U = 0$ are given, respectively, by [25]

$$S = 0.04 \pm 0.08 \quad \text{and} \quad T = 0.08 \pm 0.07. \quad (22)$$

In our case, BP4 with the largest $\Delta M = M_{H^\pm} - M_{H^0}$ in IDM gives the maximum deviation in EWPO with $\Delta S = -0.0218$ and $\Delta T = -0.0017$. These values are well within the 1σ limit of experimental uncertainty.

c. Higgs invisible decay

We note that only BP1 and BP4 have $m_h > 2m_{\text{DM}}$. Hence, the SM Higgs can decay to two DM particles for these benchmark points. The observed value of Higgs invisible branching fraction is less than 0.18 at 95% C.L. [26]. For MSSM, our branching fraction $[\text{BR}(h \rightarrow 2\tilde{\chi}^0)]$ is around 2% and 4% for BP1 and BP4, respectively. In IDM, the value of λ_L which enters into the interaction strength is kept fixed at 10^{-4} for all BPs, which helps us keep the

invisible branching ratio (BR) of $h \rightarrow H_0 H_0$ below 1% for both BP1 and BP4.

d. Higgs signal

The charged Higgs and chargino being at the electroweak scale can contribute to the loop-induced $h \rightarrow \gamma\gamma$ decay. This can affect the Higgs signal observations at the LHC in this channel. The observed value of the signal strength is constrained by ATLAS [27] as

$$\mu_{\gamma\gamma} = \frac{BR_{\text{BSM}}(h \rightarrow \gamma\gamma)}{BR_{\text{SM}}(h \rightarrow \gamma\gamma)} = 1.04_{-0.09}^{+0.10}.$$

For IDM, the maximum contribution to $BR(h \rightarrow \gamma\gamma)$ comes from BP1, which has the lightest H^+ , and the total Higgs signal strength in this particular channel with respect to the SM predictions, i.e., $\mu_{\gamma\gamma}^{\text{IDM}} = 0.975$. The deviation from the SM prediction goes down as the charged Higgs mass increases. Similarly for MSSM, BP1 gives the maximum contribution to $BR(h \rightarrow \gamma\gamma)$ with $\mu_{\gamma\gamma}^{\text{MSSM}} = 1.21$. We find that the Higgs signal strength for both IDM and MSSM are within 1σ and 2σ of the allowed signal strength, respectively.

III. SIGNAL AND BACKGROUND

The signal for our analysis comes from the pair production of the exotic charged particles (C^\pm) followed by their decay to their neutral partner (C^0) and charged gauge boson W^\pm . It is worth pointing out here that most models which are proposed to give a DM candidate in the spectrum exhibit a similar chain of production where the final state involves a pair of DM particles. The visible particle multiplicity associated with the two DM final states depends on the particle being produced in the hard scattering process. The challenging aspect of obtaining good signal sensitivity then relies on the strength with which the hard scattering process takes place. Producing electroweak strength particles at LHC leads to very weak sensitivities and, therefore, makes the spin determination very difficult. We, therefore, consider their production at ILC in the simplest and most obvious mode of production process. We choose the channel where one of the W decays leptonically while the other one decays hadronically, i.e.,

$$\begin{aligned} e^+ e^- \rightarrow C^+ C^-, \quad C^\pm \rightarrow C^0 W^\pm, \quad W^\pm \rightarrow l^\pm \nu_l / \bar{\nu}_l, \\ W^\mp \rightarrow jj, \end{aligned} \quad (23)$$

forming a final state of $l^\pm 2j + E_T$. The Feynman diagram up to W^\pm production is shown in Fig. 1. The signal process in IDM and MSSM, along with the SM background, is described below.

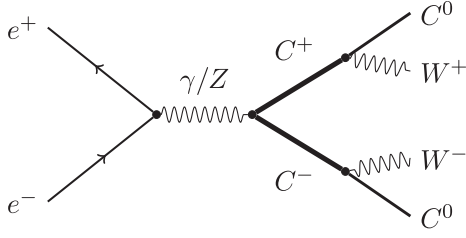


FIG. 1. Representative Feynman diagram for the signal process $e^+e^- \rightarrow C^+C^- \rightarrow W^+W^-2C^0$.

A. IDM signal

In IDM, H^+H^- is produced via two s -channel processes with the Z boson and γ as mediators from initial e^-e^+ . Then H^\pm decay to $W^\pm H_0$, where H_0 is stable, while the W boson decays to lepton and hadrons producing one lepton, two jets, and missing energy final states. We have kept the pseudoscalar A_0 mass higher than H^\pm . Since there are no other lighter particles which are Z_2 odd, the BR of H^\pm to $W^\pm H_0$ channel will be 100%. The two DM particles H_0 and neutrino act as the source of missing energy.

B. MSSM signal

In MSSM, similar s -channel diagrams can produce the lightest chargino χ_1^\pm at ILC. Although there is a possibility of a t -channel diagram due to a sneutrino, we assume that all scalar superpartner masses are very heavy including the sneutrino, which is kept at a mass of 12 TeV. Hence, the contribution from the sneutrino exchange will be much suppressed due to the large mass of sneutrino. The charginos then decay to $W^\pm \chi_0$ and further decay of W^\pm as before, giving the desired final states with the neutralinos now playing the role of DM. For our analysis, we have taken all R_p odd particles except the lightest neutralino heavier than the mass of χ_1^\pm which again gives its decay BR to $W^\pm \chi_0$ as 100%. Here, too, the missing energy gets a contribution from the two DM states χ_0 and a neutrino.

C. SM background

The dominant background for our signal is the W^+W^- production in SM, where one W boson decays leptonically while the other one decays hadronically. There are three major subprocesses in SM contributing to W^-W^+ production, with two being s -channel processes having a photon and Z boson propagator and the other and most dominant t -channel process with the light neutrino running in the propagator. The W^-W^+Z production with $Z \rightarrow \nu\bar{\nu}$ also produces the same final state, but this background is negligibly small (roughly 100 times smaller in cross section than W^+W^- production) due to an additional electroweak coupling and phase-space suppression. Additionally, the small branching for $Z \rightarrow \nu\bar{\nu}$ decay also makes the contributions from this process weaker. We can, therefore,

safely ignore the W^-W^+Z contributions for the background in our analysis.

We wish to study the polarization and spin of the intermediate exchanged as well as produced particles. We have generated the signal and background events in the package WHIZARD [28] at ILC with $\sqrt{s} = 1$ TeV center of mass energy. We generate the events with the initial state radiation (ISR) effect switched on. During the event generation, we have put a set of inclusive cuts with $P_{T_{j_1, j_2, l}} > 10$ GeV and the invariant mass of jets M_{jj} to lie between 60 and 100 GeV. Then the simulated events are showered in PYTHIA8 [29] for energy smearing effects. After the hadronization of the final state jets, we perform the fast detector simulation in DELPHES-3 [30] with the International Linear Detector card. Events are selected at the detector level with the following selection cuts:

$$\begin{aligned} p_{T_j} > 30 \text{ GeV}, & \quad p_{T_l} > 30 \text{ GeV}, \\ E'_T > 30 \text{ GeV}, & \quad 60 \text{ GeV} < M_{jj} < 100 \text{ GeV}, \\ |\eta_j| < 4.5, & \quad |\eta_l| < 2.5, \quad \Delta R_{j,j} > 0.5, \\ \Delta R_{l,l} > 0.5, & \quad \Delta R_{l,j} > 0.5. \end{aligned} \quad (24)$$

We name these cuts as Sel_cut.

IV. SIGNAL ANALYSIS AT ILC WITH BEAM POLARIZATION

We now present our signal analysis using polarized beams in the initial states. Initial state polarization is a useful diagnostic at the ILC, and, by adjusting initial state polarizations, one can select specific states preferentially. In this work, we present our analysis by using the option of using both e^- and e^+ beams longitudinally polarized as well as having them transversely polarized. Since we want to show how the spin of the newly produced particles could show up in some kinematic variables, it is useful to find out which polarization option will be best suited to help identify such states with better confidence.

Unlike the LHC, where the parton collisions are over a range in center of mass energies, we know that ILC will have a more or less fixed center of mass energy for the e^-e^+ collisions. A small spread in the collision energy, however, arises from ISR at the ILC, which is the most important QED correction to the Born cross section [31]. Bremsstrahlung effects are an important source of ISR, and it is the radiation caused by the interaction between the electron and positron participating in the annihilation event at e^+e^- colliders. Thus, its effects must be considered for realistic simulation to study physics signals at future linear colliders such as the ILC. The radiative corrections to processes with arbitrary final states need evaluation to achieve precision measurements. The ISR photons are generally soft with small transverse momenta, so they eventually escape detection. However, their effect is imprinted in the physics analysis

through modification of the colliding beam energies and an effective boost along the beam axis for the final states. For a realistic analysis, we, therefore, include the ISR effects in our study. A somewhat subdominant correction for the center of mass energy also comes from another phenomenon called beamstrahlung which we have neglected.

A. Analysis with longitudinal beam polarization

We perform our collider analysis in the chosen final state with longitudinal beam polarization (Lpol) of initial e^\pm beams primarily because of the larger cross sections than with the unpolarized (Unpol) beams; The degree of polarization for (e^- , e^+) beams are chosen to be (-80% , $+60\%$). The SM WW background has a cross section of about 680.954 fb in Unpol and 1957.84 fb in Lpol with generation-level cuts given in Eq. (24). The larger cross sections are effectively due to the choice of polarization that enhances left-handed current contribution.

The cross sections of the signal are larger in Lpol too, compared to Unpol in all four BPs, shown in Table II, by roughly the same factor by which the background cross section is larger in Lpol compared to Unpol. Thus, signal significance improves in Lpol than in Unpol, even without any kinematic cuts to reduce SM background. From Table II, it follows that IDM has $\mathcal{O}(1)$ less cross section than MSSM. This can be understood in the following way. In the massless limit (boost $\beta \rightarrow 1$), for the photon-mediated diagram, the total pair production cross section of H^\pm is 4 times smaller than the pair production cross section of χ_1^\pm at an electron-positron collider. The reason for the enhanced cross section of χ_1^\pm pair production is that there are four ways of combining helicity states of χ_1^\pm and e^\pm , while for the scalar there is only one degree of freedom for H^\pm each. The production cross section for a pair of fermions again goes up when we consider them to be massive. For the photon-mediated diagram, the cross sections follow as

$$\begin{aligned}\sigma(e^-e^+ \rightarrow H^-H^+) &\propto \frac{2}{3}e^4\beta^3 \quad \text{and} \\ \sigma(e^-e^+ \rightarrow \chi_1^-\chi_1^+) &\propto -\frac{4}{3}e^4\beta(-3 + \beta^2)\end{aligned}\quad (25)$$

for unpolarized initial beams [see Eqs. (B25), (B35), and (B16)]. Similarly for the diagram with a Z -boson propagator, the factor associated with a Z -boson vertex ($T_3 - \sin^2\theta_W Q$) is larger for a chargino than the charged Higgs. In our case, the lightest chargino is wino dominated. Following the notation in Appendix B, the ratio between the production cross section of the chargino pair and the charged Higgs pair is $4(a_\chi^2 + v_\chi^2)/(g_2 \cos\theta_W - g_1 \sin\theta_W)^2 = 27.24$ for an unpolarized beam in the $\beta \rightarrow 1$ limit. The individual cross section from the photon and the Z diagrams are of the same order, and they interfere destructively. Considering both the photon and the Z -mediated diagram, we get chargino pair production cross section nearly 8 times larger than the charged Higgs pair production cross section for an unpolarized beam in the $\beta \rightarrow 1$ limit. This ratio increases further when we consider the final state particles to be massive. However, it should be noted that, in generic scenarios not restricted to SUSY where interactions with such exotics emerge from suppressed mixing angles, smaller branching fractions in the decay modes or additional subprocesses contributing destructively can lead to somewhat comparable cross sections with the scalar production. Nevertheless, the large cross section for the fermion production is always a good discriminator when compared to scalar production in simple setups.

(a) *Kinematic variables.*—The role of kinematic variables to analyze the signal against the SM background, which naturally arises in the final state $l^\pm 2j + \cancel{E}_T$, are missing transverse energy (\cancel{E}_T), transverse momentum of lepton and jets (p_{T_l} , $p_{T_{j_1}}$, $p_{T_{j_2}}$), total visible mass ($M_{l_{j_1}j_2}$), and energy of the jj pair which reconstructs the W boson energy (E_W) and lepton (E_l). Normalized distribution of these kinematic variables is shown in Fig. 2 for BP1 as representative with longitudinally polarized beams at 1 TeV ILC set up for both IDM (dashed blue line) and MSSM (dotted red line) signal and SM background (solid green line).

The \cancel{E}_T distribution (left-top panel in Fig. 2) shows a peak in the lower energy values for the SM background compared to the signal. This is because the source of \cancel{E}_T in the SM is the neutrino coming from the W boson decay, while for the signal, we have additional contributions coming from the undetected stable exotics C^0 along with

TABLE II. The cross sections of signal for the final state $e^-e^+ \rightarrow l^\pm + 2j + \cancel{E}_T$ after the basic generation level cuts.

Benchmark	Mass(M^\pm, M_0) (GeV)	IDM cross section (fb)		MSSM cross section (fb)	
		Unpol	Lpol	Unpol	Lpol
BP1	(160, 60)	5.911	14.331	55.163	158.900
BP2	(220, 100)	4.996	12.103	54.959	158.136
BP3	(220, 120)	5.006	12.146	54.799	157.702
BP4	(300, 10)	3.699	8.966	54.445	156.363

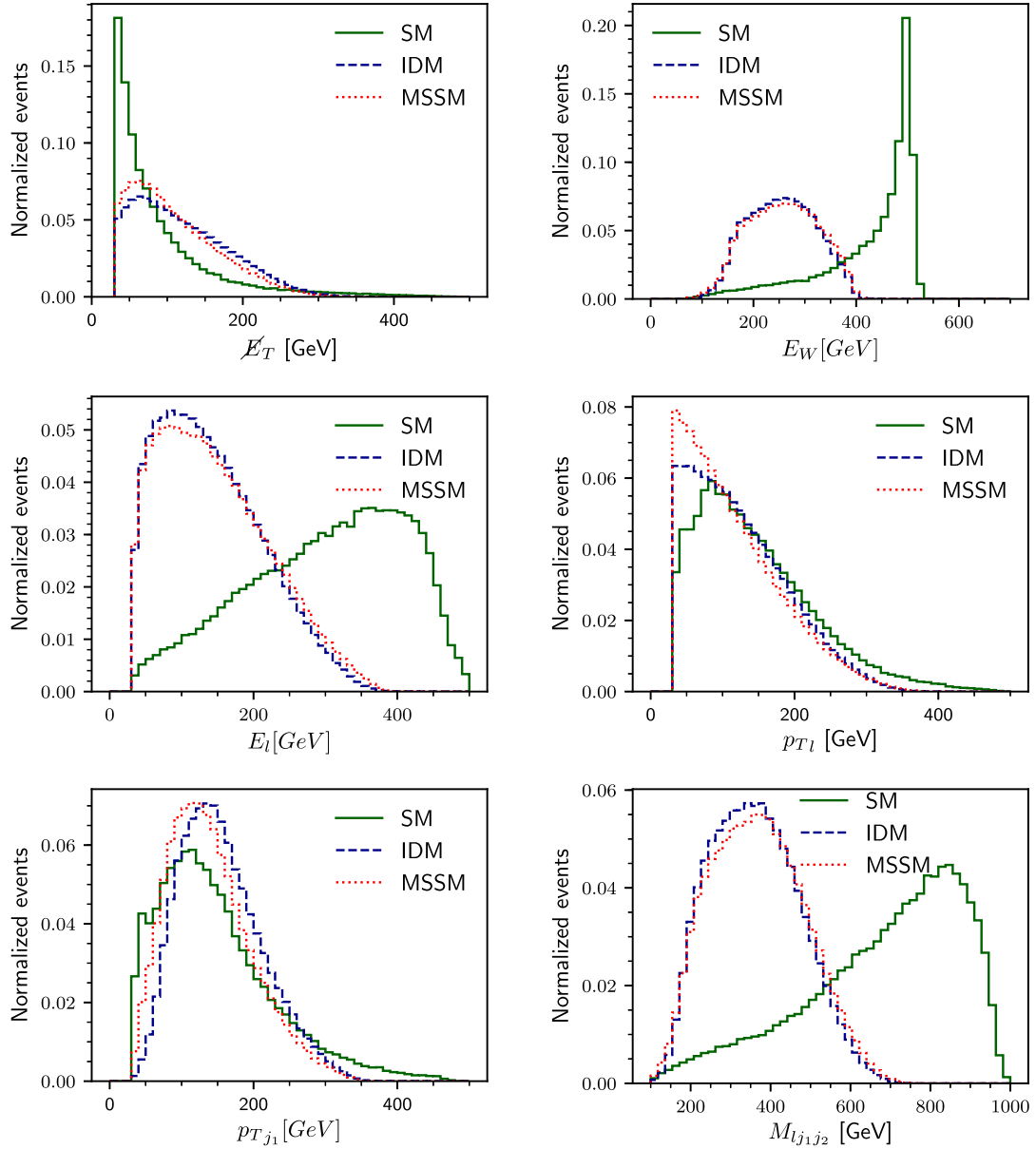


FIG. 2. Normalized distributions of kinematic variables in $e^-e^+ \rightarrow l^\pm + 2j + \cancel{E}_T$ with $\sqrt{s} = 1$ TeV and longitudinal polarized beams for BP1.

a neutrino. Furthermore, in the case of signal, the peak of \cancel{E}_T shifts toward higher values as the splitting between the mass of the charged exotic and the stable neutral particle (ΔM) increases, which can be seen in Fig. 3, where the SM background along with all four BPs of IDM and MSSM is shown. The peak for BP1 and BP3 with $\Delta M = 100$ GeV are at the same energy, while the peaks for BP2 ($\Delta M = 120$ GeV) and BP4 ($\Delta M = 290$ GeV) are at the higher energy side in \cancel{E}_T distribution due to more availability of energy for missing C^0 in the rest frame of its charged partner.

We note that the two jets in the signal as well as the SM background come from the W boson decay. Therefore, it is

possible to reconstruct the energy of the W using the two jets. Ideally, for the SM background, the W bosons should be produced back to back with $E_W = \sqrt{s}/2 = 500$ GeV. However, the ISR effect gives an effective boost as well as changes the hard scattering collision energy, which, along with hadronization and detector effects, result in the smearing of energies for the W boson (jj pair) and lepton as well as a longish tail in the energy distribution of E_W extending to the kinematic threshold of $\sqrt{s_{\text{eff}}} \geq 2M_W$ of the process. On the other hand, in the case of signal, the W boson is produced from the decay of C^\pm , along with missing C^0 . The available energy for W is much lower than that of SM and is highlighted in the energy distribution for

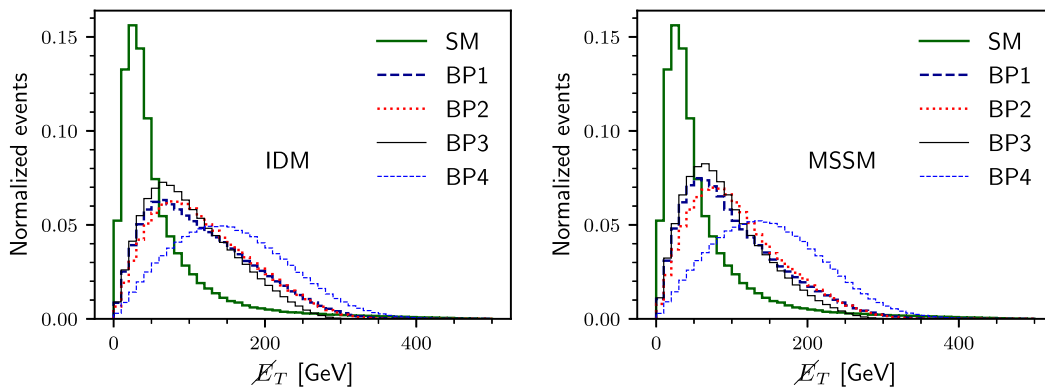


FIG. 3. Normalized distribution of E_T for all four BPs of the IDM and MSSM along with SM background in $e^-e^+ \rightarrow l^\pm + 2j + E_T$ with $\sqrt{s} = 1$ TeV and longitudinal polarized beams.

E_W . The difference between the end point of E_W in SM and BSM models will be at least the C^0 mass. Similarly, the presence of missing C^0 can be seen from its imprint in other kinematic variables as well, given by E_l , M_{l,j_1,j_2} , and P_T 's of jets and lepton, where the end point in these distributions for the signal shifts toward the low-energy values as compared to SM background. Hence, rejection cuts near the end point of these variables help reduce the SM background significantly while keeping enough statistics for the signal.

We, thus, implement a set of cuts on these kinematic variables as $E_T > 50$ GeV, $P_{T_{l,j_1}} < 400$ GeV, $M_{l,j_1,j_2} < 700$ GeV, $E_l < 400$ GeV, and $E_W < 400$ GeV to reduce the SM background while keeping enough statistics for the signal. We name these sets of cuts as Kin_cut.

(b) *Angular variables.*—It is quite well known that particle spin dictates the Lorentz structure of interaction vertices, and an efficient way of identifying these properties is through observing the kinematics in the angular variables of final state particles. For a scattering process such as

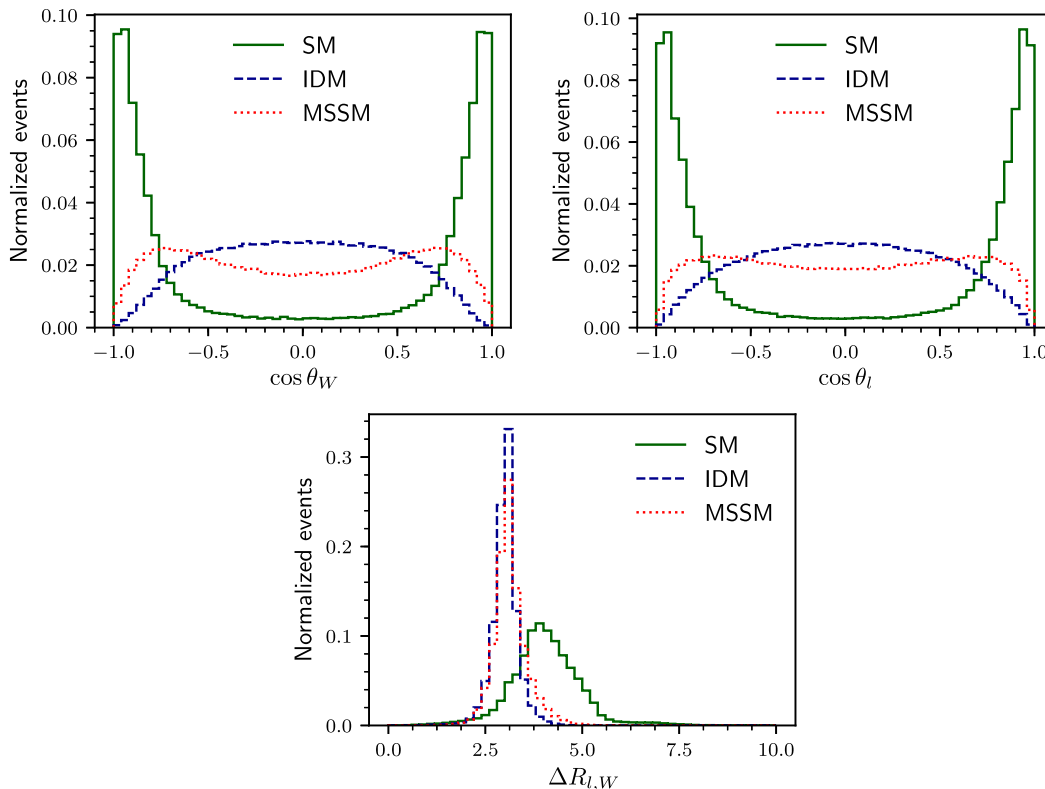


FIG. 4. Normalized distribution of angular variables in $e^-e^+ \rightarrow l^\pm + 2j + E_T$ with $\sqrt{s} = 1$ TeV and longitudinal polarized beams for BP1.

TABLE III. The cut-flow information on the $e^-e^+ \rightarrow l^+ + 2j + \cancel{E}_T$ process for both the signals and background along with the significances for all four BPs at the 1 TeV ILC for 100 fb^{-1} of integrated luminosity.

Cuts	SM background	IDM signal				MSSM signal			
	W^+W^-	BP1	BP2	BP3	BP4	BP1	BP2	BP3	BP4
Sel_cut	22709.6	558.29	462.28	456.62	321.47	5517.66	5337.85	4948.52	5743.17
Sel_cut + Kin_cut	3256.22	491.49	420.57	400.05	295.14	4738.46	4789.66	4224.54	5153.8
Sel_cut + Kin_cut + Ang_cut	1942.75	479.75	410.05	392.64	274.70	4318.11	4352.4	3924.35	4497.23
	Significance (S)	10.47	9.00	8.63	6.09	77.56	78.08	71.55	80.25

$e^+e^- \rightarrow f\bar{f}$, where f is a stable SM fermion, it is clearly highlighted in the polar distributions of the final state fermion. However, it becomes more challenging if the final state particles come from cascade decay of unstable particles produced as primaries in the e^+e^- collisions, as in our case. We, therefore, explore the properties by looking at the normalized distributions of some angular variables such as $\cos\theta$ of W (jj pair) and lepton and the isolation variable $\Delta R = \sqrt{\Delta\eta^2 + \Delta\phi^2}$ between the lepton and W , which are shown in Fig. 4 for the SM background and signal (IDM and MSSM) for BP1 as representative. Owing to a t -channel subprocess in the SM process, $\cos\theta_W$ sharply peaks at ± 1 , i.e., along with the beam directions: The W^- tends to remain toward the e^- direction, while the W^+ tends to remain toward the e^+ direction; see left-top panel in Fig. 4. On the other hand, there are only two s -channel subprocesses in the IDM signal, which makes the $\cos\theta_W$ peak at 0, i.e., transverse to the beam directions. In the case of the MSSM signal, there could be a t -channel subprocess due to the sneutrino, which is kept heavy not to contribute to our analysis. Thus, the $\cos\theta_W$ distribution has a small peak near ± 1 with an overall flat shape throughout. The angular behavior of W transfers to its decay product, and, thus, the lepton's $\cos\theta$ distribution is of similar nature to that of W ; see right-top panel. So an inclusion cut of $|\cos\theta| < 0.9$ for the lepton and the W will be effective to suppress the background with less effect on signals. In SM, the two intermediate W 's are boosted in opposite directions,

while in the case of signals, the W 's are less boosted and also not in opposite directions, as they are decayed from C^\pm together with C^0 's. Hence, the $\Delta R_{l,W}$ attains higher values as compared to that of signals; see the bottom panel in Fig. 4. We, thus, put a rejection cut of $\Delta R_{l,W} > 5.0$ to reduce SM background with less effect on the signals. We name the set of cuts on the angular variables as Ang_cut.

We estimate signal significance with an integrated luminosity of $\mathcal{L} = 100 \text{ fb}^{-1}$ with the formula

$$S = \sqrt{2 \left[(S+B) \log \left(1 + \frac{S}{B} \right) - S \right]} \quad (26)$$

with S being the number of signal events and B being the number of background events at a given luminosity. The signal significances of the IDM signal and MSSM signal are shown in Table III for the successive cuts on kinematic variables and angular variables in all four BPs. The significance values confirm that all four BPs are above 5σ discovery limits in our analysis.

Although there is a good distinction between the background and the signals, it is ambiguous about the spin nature of particles contained in signals apart from the fact that the MSSM signal has more significance than the IDM signal with the same mass parameters. We try to estimate how the IDM signal is different from the MSSM signal based on the asymmetry of some angular variables in the following subsection.

 TABLE IV. Asymmetries for both the signals and background and difference between the signals in the $e^-e^+ \rightarrow \ell + 2j + \cancel{E}_T$ process for longitudinally polarized beams for $\mathcal{L} = 100 \text{ fb}^{-1}$ of integrated luminosity.

Variables	\mathcal{A}_{SM}	$\mathcal{A}_{\text{SM+IDM}}$				$\mathcal{A}_{\text{SM+MSSM}}$			
	W^+W^-	BP1	BP2	BP3	BP4	BP1	BP2	BP3	BP4
$\cos\theta_W$	0.1682	0.0632619	0.0663791	0.0573263	0.118111	0.0260318	-0.030412	-0.0775697	-0.00320661
$\cos\theta_l$	0.291	0.169782	0.182949	0.180954	0.225528	0.0212554	-0.0130694	-0.0379408	0.0206557
	$\delta\mathcal{A}_{\text{SM}}$	$\left \frac{\Delta\mathcal{A}}{\delta\mathcal{A}_{\text{SM}}} \right $							
	W^+W^-	BP1	BP2	BP3	BP4	BP1	BP2	BP3	BP4
$\cos\theta_W$	0.0223	1.66469	4.32789	6.0317	5.42458				
$\cos\theta_l$	0.0217	6.84267	9.03066	10.0846	9.43857				
χ^2		49.5933	100.2823	138.0805	118.5126				

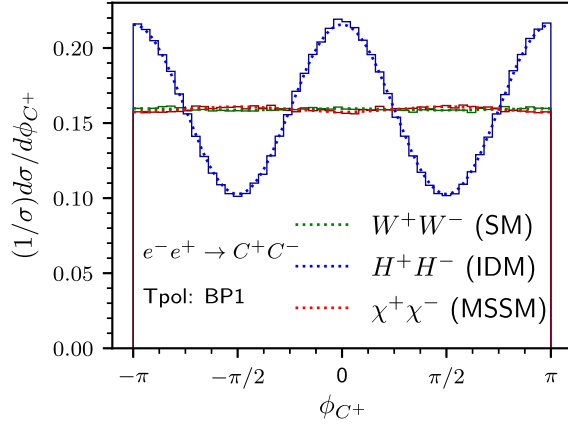


FIG. 5. Normalized distribution of the azimuthal angle ϕ of the charged particle (C^+) at production level for the background and the signals in BP1 in e^-e^+ collider with transversely polarized beams at $\sqrt{s} = 1$ TeV.

1. Identifying the nature of signal

We now try and identify the spin nature of the exotic charged particle (C^+) and its partner (C^0) by taking account of the observations made in the previous subsection. We try to identify the type of signal based on asymmetries constructed from the angular variables $\cos\theta_W$ and $\cos\theta_l$ for the signal inclusive of the background after effectively reducing the background contribution maximally as discussed earlier. Then we estimate the difference between the signal from the two models based on χ^2 using the asymmetries. We have already discussed the difference in the shapes of $\cos\theta_{W/l}$ distribution, given in Fig. 4 for the MSSM and IDM signal events. Based on the symmetric shape in $\cos\theta = 0$, we define an asymmetry for both the variables as

$$\mathcal{A}(\cos\theta_{W/l}) = \frac{\sigma(|\cos\theta_{W/l}| > 0.5) - \sigma(|\cos\theta_{W/l}| < 0.5)}{\sigma(|\cos\theta_{W/l}| > 0.5) + \sigma(|\cos\theta_{W/l}| < 0.5)}. \quad (27)$$

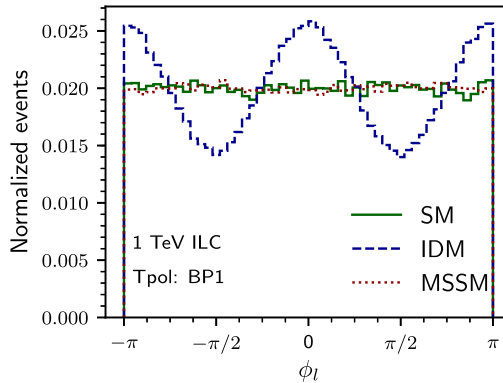
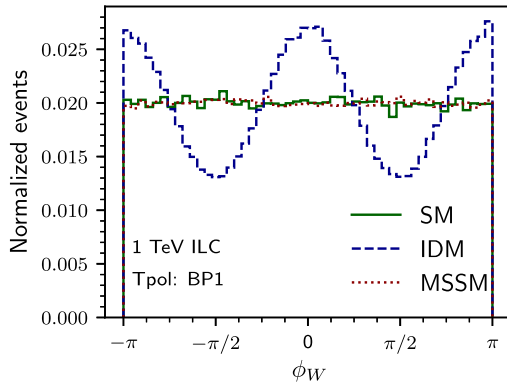


FIG. 6. Normalized distribution of ϕ_W (left panel) and ϕ_l (right panel) for the background and the signals in BP1 in e^+e^- collider for $\sqrt{s} = 1$ TeV with transversely polarized beams.

The difference is then estimated by a χ^2 , calculated as

$$\chi^2 = \sum_i \left| \frac{\Delta\mathcal{A}^i = \mathcal{A}_{\text{IDM+SM}}^i - \mathcal{A}_{\text{MSSM+SM}}^i}{\delta\mathcal{A}_{\text{SM}}^i} \right|^2, \quad (28)$$

i runs on the variables; $\delta\mathcal{A}_{\text{SM}} = \sqrt{\frac{1-\mathcal{A}_{\text{SM}}^2}{\sigma_{\text{SM}} \times \mathcal{L}}}$ is the statistical error on asymmetries due to SM background. The asymmetries in each signal are estimated including the background after putting all the cuts (Sel_cut + Kin_cut + Ang_cut), i.e., reducing maximum background so as to highlight only the signal. The asymmetry of a signal (S) including background (B) will be given as

$$\mathcal{A}_{S+B} = \frac{\mathcal{A}_S \sigma_S + \mathcal{A}_B \sigma_B}{\sigma_S + \sigma_B}, \quad (29)$$

i.e., weighted by their respective cross sections. The estimated values of asymmetries of the variables in each signal mixed with the background are shown in Table IV (top two rows). Although the \mathcal{A}_S for $\cos\theta_{W/l}$ seems to be $(-)$ for IDM signal and $(+)$ for MSSM signal by looking Fig. 4, the \mathcal{A}_{S+B} are $(+)$ for IDM, while they are $(-)$ for MSSM in most of the BP. The reasons are the following. The asymmetries in SM are large $(+)$, and the SM cross section is larger by roughly a factor of 5 compared to the cross sections in IDM after all cuts; see Table III. Hence, the asymmetries in IDM signal reduce but remain positive when combined with the SM background weighted by cross sections in accordance with Eq. (29). For the case of MSSM, individual asymmetries in signal become $(-)$ after the inclusion cut $|\cos\theta_{W/l}| < 0.9$. Moreover, the cross sections are larger in MSSM compared to SM by roughly a factor of 2; see Table III. This makes the \mathcal{A}_{S+B} to be $(-)$ for most of the BP. The changes in the asymmetries with respect to background are above 1σ statistical errors shown in the second column in Table IV. Differences between the signals are calculated in terms of χ^2 and shown in Table IV in the last three rows for all BPs for an integrated

TABLE V. Azimuthal asymmetries for both the signals and background in the $e^-e^+ \rightarrow \ell + 2j + \cancel{E}_T$ process for transversely polarized initial beams. The error in the SM is shown for $\mathcal{L} = 100 \text{ fb}^{-1}$ of integrated luminosity.

Variables	\mathcal{A}_{SM}	$\delta\mathcal{A}_{\text{SM}}$	$\mathcal{A}_{\text{SM+IDM}}$				$\mathcal{A}_{\text{SM+MSSM}}$			
			BP1	BP2	BP3	BP4	BP1	BP2	BP3	BP4
ϕ_W	-0.0029	0.0379	0.0471	0.0382	0.0387	0.0116	-0.0053	-0.0032	-0.0057	-0.0038
ϕ_l	0.0113	0.0379	0.0475	0.0378	0.0375	0.0222	-0.0018	0.0009	0.0001	0.0027

luminosity of $\mathcal{L} = 100 \text{ fb}^{-1}$. The two signals have a difference of $\sim 10\sigma$ in all the four BPs based on the total χ^2 shown in the last row.

These asymmetries can help to identify the nature of the signal if observed above the background. The asymmetries remain (+) for IDM, while they become (-) and above statistical errors for BP2 and BP3, due to having large M_0 , and (+) and within 1σ error for other BPs. Nevertheless, the characteristics of the asymmetries which can be useful to distinguish between the signals are benchmark dependent. We require a variable that can distinguish between the signals irrespective of the benchmark masses; we will explore such a possibility in the following section by using transverse beam polarizations.

B. Analysis with transverse beam polarization

We observed in the previous section that, though the angular variables $\cos\theta_W$ and $\cos\theta_l$ are useful in identifying the nature of the signal, they are limited to being dependent on benchmark selections. The transversely polarized beams have the potential of exploring new physics from the azimuthal distributions of final state particles [32–38]. Here, we use the facility of transverse polarization of e^\pm beams to showcase the distribution of azimuthal angle ϕ , which has a very distinctive nature for two signals irrespective of the benchmark selections as well as the background. Before looking at the distribution of ϕ for the final states, we first observe the distribution at the production level and make an ansatz at the final state particle. We calculate the normalized ϕ distribution for the C^+ analytically in $e^-e^+ \rightarrow C^+C^-$ process for SM as well as for the signals with transverse beam polarization of (80%, 60%) for (e^-, e^+) beams and show them in Fig. 5 for BP1 with *dotted* lines. The same distributions for ϕ_C are also shown with *solid* lines computed from events generated in WHIZARD.¹ The differential cross section in ϕ_C has the form

$$\frac{d\sigma}{d\phi_C} = \frac{\sigma}{2\pi} + \eta_T \xi_T f(\beta_C) \cos(2\phi_C - \phi_{e^-} + \phi_{e^+}), \quad (30)$$

where $f(\beta_C)$ is a function of boost (β) for the particle C with different forms for different physics model; see Appendix B for details. We choose the spin direction for

both the initial beams along the (+) x axis as an example; making the spin directions opposite for the two beams would result in an overall phase shift for all models, not affecting our findings. The explicit form of $f(\beta_C)$ [shown in Eqs. (B18), (B29), and (B39) for analytical expressions] makes the amplitude large for the IDM signal while negligibly small for the MSSM signal and the W^+W^- background; see Fig. 5. If the ϕ_C distribution in MSSM attains an amplitude comparative to IDM in some other benchmark scenario, the nature will be different due to having a relative π phase shift compared to IDM, as can be seen in Fig. 5. This behavior of ϕ distribution for the mother particle C^+ is transferred to its decay products, which in this case are the lepton and $W(jj)$ even after including the detector level effects as well as with ISR effect, as seen in Fig. 6. Here also, the amplitude in IDM is large enough compared to MSSM and SM, making the $\phi_{W/l}$ a good discriminator for identifying the nature of the signal. To depict a quantitative measure of distinction between the two signals, we again construct asymmetries for the $\phi_{W/l}$ given by

$$\mathcal{A}(\phi_{W/l}) = \frac{\sigma(\cos(2\phi_{W/l}) > 0) - \sigma(\cos(2\phi_{W/l}) < 0)}{\sigma(\cos(2\phi_{W/l}) > 0) + \sigma(\cos(2\phi_{W/l}) < 0)}. \quad (31)$$

We have listed the asymmetry values in Table V for the SM background as well as all four BPs combined with the background after the cuts Sel_cut + Kin_cut + Ang_cut, as used in the previous section for our analysis with longitudinally polarized beams. The asymmetries for both ϕ_W and ϕ_l are nearly zero (much smaller than the 1σ statistical error given in the first and second rows of the second column) for the background (shown in the second column) and the MSSM signal. The asymmetries for the IDM combined with the background, however, remain large enough even after mixing with the background with a larger cross section compared to the signal. Although the asymmetry in IDM reduces as the m_H increases [see Eq. (B29) for the phi analytic] mainly due to smaller cross sections, asymmetry can still be significant enough with higher integrated luminosity. Thus, these two distributions and their asymmetries are able to identify the spin nature of C^+/C^0 contained in the signal if a significant deviation is

¹ISR effect has been neglected here for simplicity.

observed at a future ILC. The signal identification can be quantified with higher significance for higher luminosity.

V. CONCLUSION

In this article, we make an effort to identify the spin nature of exotic charged particles and their neutral partner, possibly a dark matter candidate, in the $l^\pm 2j + \vec{E}_T$ final state at the future e^+e^- collider. We chose two well-known BSM models such as IDM and MSSM, containing exotic charged particles and neutral partners of spin zero (scalar) and half (fermion), respectively, for the demonstration. First, we devised some rectangular cuts on some kinematic as well as angular variables to reduce the SM background in order to find a significant deviation from the SM background. We then use the shape of angular variables and their asymmetries to identify the nature of the new physics signals. The $\cos\theta_{W/l}$ distribution and their asymmetries help distinguish and identify the MSSM and the IDM signals over the SM backgrounds with longitudinally polarized beams depending on the benchmark points. The transverse beam polarization helps to identify the IDM signal robustly through the azimuthal ($\phi_{W/l}$) distribution of the final state particles. Thus, both longitudinal polarization and transverse polarization prove useful in their respective ways in identifying the spin nature of exotic charged particles and their partner contained in a new physics signal if observed at a future e^-e^+ collider in the

$l^\pm 2j + \vec{E}_T$ final state. We note that, while the identification gets help from the enhanced cross section in the longitudinal polarization due to the large cross section, a more clear and more distinct identification is established with the use of transversely polarized beam.

ACKNOWLEDGMENTS

The authors acknowledge the support from Department of Atomic Energy (DAE), India for the Regional Centre for Accelerator based Particle Physics (RECAPP), Harish Chandra Research Institute.

APPENDIX A: FEYNMAN RULES

The Feynman rules for the vertices involved in the SM, IDM, and MSSM processes are

- (i) $H^+(k_1)H^-(k_2)A_\mu: -ie(k_2 - k_1)_\mu$,
- (ii) $H^+(k_1)H^-(k_2)Z_\mu: -i(-g_1 \sin\theta_W + g_2 \cos\theta_W)(k_2 - k_1)_\mu$,
- (iii) $\chi_1^+\chi_1^-A_\mu: -ie\gamma_\mu$,
- (iv) $\chi_1^+\chi_1^-Z_\mu: i\gamma_\mu(v_\chi - a_\chi\gamma_5) = ig_Z\gamma_\mu((g_L + g_R) + (g_R - g_L)\gamma_5)$,

where $g_L = (\sin^2\theta_W - \frac{3}{4} - \frac{1}{4}(2\cos^2\theta_L - 1))$, $g_R = (\sin^2\theta_W - \frac{3}{4} - \frac{1}{4}(2\cos^2\theta_R - 1))$, and $\cos\theta_L = \mathcal{U}_{11}$ and $\cos\theta_R = \mathcal{V}_{11}$ are the cosine of left and right chargino mixing angles, respectively.

APPENDIX B: AZIMUTHAL ANGULAR DISTRIBUTION WITH TRANSVERSELY POLARIZED BEAMS

1. SM: $e^-(p_1, s_1)e^+(p_2, s_2) \rightarrow W^-(k_2, \lambda_2)W^+(k_1, \lambda_1)$

The amplitude for the diagram with the photon in the s channel is given by

$$\mathcal{M}_\gamma(s_1, s_2, \lambda_1, \lambda_2) = -\frac{ie^2}{s} \bar{v}(s_2, p_2)\gamma^\mu u(s_1, p_1)\epsilon^\nu(\lambda_1, k_1)\epsilon^{\rho*}(\lambda_2, k_2)G_{\mu\nu\rho}(k_1, k_2), \quad (\text{B1})$$

where

$$G_{\mu\nu\rho}(k_1, k_2) \equiv ((k_2 - k_1)_\mu g_{\nu\rho} - (2k_2 + k_1)_\nu g_{\rho\mu} + (2k_1 + k_2)_\rho g_{\mu\nu}). \quad (\text{B2})$$

Following are the expressions for the amplitudes of the diagrams containing a Z boson and neutrino propagator, respectively:

$$\mathcal{M}_Z(s_1, s_2, \lambda_1, \lambda_2) = \frac{ie^2}{2(s - M_Z^2)\sin^2\theta_W} \bar{v}(s_2, p_2)\gamma^\mu(v_f - a_f\gamma_5)u(s_1, p_1)\epsilon^\nu(\lambda_1, k_1)\epsilon^{\rho*}(\lambda_2, k_2)G_{\mu\nu\rho}(k_1, k_2), \quad (\text{B3})$$

$$\mathcal{M}_\nu(s_1, s_2, \lambda_1, \lambda_2) = -\frac{ig_2^2}{(p_1 - k_1)^2} \bar{v}(s_2, p_2)\gamma^\mu P_L(\not{p}_1 - \not{k}_1)\gamma^\mu P_L u(s_1, p_1)\epsilon^\mu(\lambda_1, k_1)\epsilon^{\nu*}(\lambda_2, k_2). \quad (\text{B4})$$

The square amplitude with polarized initial beams is given by

$$|\mathcal{M}|^2 = \sum_{s_i, \lambda_j} \mathcal{M}(s_1, s_2, \lambda_1, \lambda_2)\mathcal{P}_{e^-}(s_1, s_3)\mathcal{P}_{e^+}(s_2, s_4)\mathcal{M}^\dagger(s_3, s_4, \lambda_1, \lambda_2), \quad (\text{B5})$$

where

$$\mathcal{M} = \mathcal{M}_\gamma + \mathcal{M}_Z + \mathcal{M}_\nu. \quad (\text{B6})$$

The spin density matrix for the electron and positron (\mathcal{P}_{e^-} and \mathcal{P}_{e^+} , respectively) is written as

$$\mathcal{P}_{e^-} = \begin{pmatrix} \frac{1}{2} & \frac{1}{2} e^{-i\phi_{e^-}} \eta_T \\ \frac{1}{2} e^{i\phi_{e^-}} \eta_T & \frac{1}{2} \end{pmatrix}, \quad (\text{B7})$$

$$\mathcal{P}_{e^+} = \begin{pmatrix} \frac{1}{2} & \frac{1}{2} e^{-i\phi_{e^+}} \xi_T \\ \frac{1}{2} e^{i\phi_{e^+}} \xi_T & \frac{1}{2} \end{pmatrix} \quad (\text{B8})$$

with their degree of polarization along transverse direction ($\theta = \frac{\pi}{2}$, ϕ_{e^-/e^+}) as (η_T, ξ_T) , respectively,

Throughout the calculation, we use $c\theta$ and $s\theta$ as shorthand notations for $\cos \theta$ and $\sin \theta$, respectively. The total square amplitude can be written as

$$|\mathcal{M}|^2 = |\mathcal{M}_\gamma|^2 + |\mathcal{M}_Z|^2 + |\mathcal{M}_\nu|^2 + 2\text{Re}(\mathcal{M}_\gamma \mathcal{M}_Z^\dagger) + 2\text{Re}(\mathcal{M}_\gamma \mathcal{M}_\nu^\dagger) + 2\text{Re}(\mathcal{M}_\nu \mathcal{M}_Z^\dagger). \quad (\text{B9})$$

The expressions for the square amplitude of various diagrams and their interference are given by

$$\begin{aligned} |\mathcal{M}_\gamma|^2 &= \frac{1}{2(\beta^2 - 1)^2} [\beta^2 e^4 (3\beta^4 - 18\beta^2 - (3\beta^4 - 2\beta^2 + 3)c\theta^2 + 19) \\ &\quad - \beta^2 (3\beta^4 - 2\beta^2 + 3)(c\theta^2 - 1) e^4 \eta_T \xi_T \cos(2\phi) \cos(\phi_{e^-} - \phi_{e^+}) \\ &\quad - \beta^2 (3\beta^4 - 2\beta^2 + 3)(c\theta^2 - 1) e^4 \eta_T \xi_T \sin(2\phi) \sin(\phi_{e^-} - \phi_{e^+})], \end{aligned} \quad (\text{B10})$$

$$\begin{aligned} |\mathcal{M}_Z|^2 &= \frac{2\beta^2 E_e^4 e^4}{\sin^4 \theta_W (\beta^2 - 1)^2 (s - M_Z^2)^2} [(a_f^2 + v_f^2)(3\beta^4 - 18\beta^2 - (3\beta^4 - 2\beta^2 + 3)c\theta^2 + 19) \\ &\quad + (3\beta^4 - 2\beta^2 + 3)(c\theta^2 - 1) \eta_T \xi_T (a_f^2 - v_f^2) \cos(2\phi) \cos(\phi_{e^-} - \phi_{e^+}) \\ &\quad - (3\beta^4 - 2\beta^2 + 3)(c\theta^2 - 1) \eta_T \xi_T (a_f^2 - v_f^2) \sin(2\phi) \sin(\phi_{e^-} - \phi_{e^+})], \end{aligned} \quad (\text{B11})$$

$$\begin{aligned} |\mathcal{M}_\nu|^2 &= \frac{e^4}{4 \sin^4 \theta_W (\beta^4 - 2\beta^3 c\theta + 2\beta c\theta - 1)^2} [(\beta^6 - 10\beta^4 + 9\beta^2 - 4\beta^4 c\theta^4 + 4(\beta^5 + \beta^3)c\theta^3) \\ &\quad - ((5\beta^6 + 6\beta^4 - 11\beta^2)c\theta^2 + 4(3\beta^4 - \beta^2 - 4)\beta c\theta + 4)], \end{aligned} \quad (\text{B12})$$

$$\begin{aligned} \text{Re}(\mathcal{M}_\gamma \mathcal{M}_Z^\dagger) &= \frac{2\beta^2 E_e^2 e^4}{2 \sin^2 \theta_W (\beta^2 - 1)^2 (s - M_Z^2)} [v_f (18\beta^2 - 3\beta^4 + (3\beta^4 - 2\beta^2 + 3)c\theta^2 - 19) \\ &\quad + (3\beta^4 - 2\beta^2 + 3)(c\theta^2 - 1) \eta_T \xi_T v_f \cos(2\phi) \cos(\phi_{e^-} - \phi_{e^+}) \\ &\quad + (3\beta^4 - 2\beta^2 + 3)(c\theta^2 - 1) \eta_T \xi_T v_f \sin(2\phi) \sin(\phi_{e^-} - \phi_{e^+})], \end{aligned} \quad (\text{B13})$$

$$\begin{aligned} \text{Re}(\mathcal{M}_\gamma \mathcal{M}_\nu^\dagger) &= \frac{\beta^2 e^4}{4 \sin^2 \theta_W (\beta^2 - 1)^2 (2\beta c\theta - \beta^2 - 1)} [(2\beta^2 - 3\beta^4 - 3)c\theta^2 + (3\beta^4 - 18\beta^2 + 19) + 2(\beta^3 + \beta^1)c\theta^3 \\ &\quad + \beta^2 e^4 \eta_T \xi_T (2(\beta^3 + \beta)c\theta^3 + (3\beta^4 - 2\beta^2 + 3)s\theta^2) \cos(2\phi) \cos(\phi_{e^-} - \phi_{e^+}) \\ &\quad + \eta_T \xi_T (2(\beta^3 + \beta)c\theta^3 + (3\beta^4 - 2\beta^2 + 3)s\theta^2) \sin(2\phi) \sin(\phi_{e^-} - \phi_{e^+}) \\ &\quad - \eta_T \xi_T (2(\beta^3 + \beta)c\theta) \cos(2\phi) \cos(\phi_{e^-} - \phi_{e^+}) + (6\beta^4 - 2\beta^2 - 8)c\theta \\ &\quad - \eta_T \xi_T (2(\beta^3 + \beta)c\theta) \sin(2\phi) \sin(\phi_{e^-} - \phi_{e^+})], \end{aligned} \quad (\text{B14})$$

$$\begin{aligned}
Re(\mathcal{M}_\nu \mathcal{M}_Z^\dagger) = & \frac{\beta E_e^2 e^4}{2 \sin^4 \theta_W (\beta^2 - 1)^2 (2\beta c\theta - \beta^2 - 1)(s - M_Z^2)} [\beta(a_f + v_f)(2(\beta^3 + \beta)c\theta^3) \\
& + \beta(a_f + v_f)3\beta^4 s\theta^2 - (18\beta^2 - 19) \\
& + \eta_T \xi_T (a_f - v_f)((3\beta^4 - 2\beta^2 + 3)s\theta^2) \cos(2\phi) \cos(\phi_{e^-} - \phi_{e^+}) \\
& + \beta \eta_T \xi_T (a_f - v_f)((3\beta^4 - 2\beta^2 + 3)s\theta^2) \sin(2\phi) \sin(\phi_{e^-} - \phi_{e^+}) \\
& + (a_f + v_f)((2\beta^3 - 3\beta)c\theta^2 + (6\beta^4 - 2\beta^2 - 8)c\theta) \\
& - \beta \eta_T \xi_T (2(\beta^3 + \beta)c\theta s\theta^2) \sin(2\phi) \sin(\phi_{e^-} - \phi_{e^+}) \\
& - \beta \eta_T \xi_T (2(\beta^3 + \beta)c\theta s\theta^2) \cos(2\phi) \cos(\phi_{e^-} - \phi_{e^+})]. \tag{B15}
\end{aligned}$$

Here, β is the boost of the W bosons and $\sqrt{s} = 2E_e$ is the center of mass energy. Integrating over the polar angle θ , we get the differential cross section with respect to the azimuthal angle (ϕ) as

$$\frac{d\sigma}{d\phi} = \frac{\beta}{64\pi^2 s} \int d\cos\theta |\mathcal{M}|^2 \times (3.894 \times 10^{11}) \text{ fb.} \tag{B16}$$

In this case,

$$\begin{aligned}
\frac{d\sigma}{d\phi} = & \frac{\beta \times 3.894 \times 10^{11}}{64\pi^2 s} \left(\frac{E_e^2 e^4 (a_f + v_f)(4\beta(3\beta^6 - 23\beta^4 + \beta^2 + 27))}{12\beta M_W^4 (s - M_Z^2)} \right. \\
& + \frac{E_e^2 \eta_T e^4 \xi_T (a_f - v_f)(3(\beta^2 - 1)^4 \log(\frac{1+\beta}{1-\beta})^2) \cos(2\phi - \phi_{e^-} + \phi_{e^+})}{12\beta M_W^4 (s - M_Z^2) \sin^4 \theta_W} \\
& + \frac{16\beta^3 e^4 (3\beta^4 - 26\beta^2 + (3\beta^4 - 2\beta^2 + 3)\eta_T \xi_T \cos(2\phi - \phi_e + \phi_p) + 27)}{24\beta M_W^4} + \frac{8\beta^2 E_e^4 e^4 ((3\beta^4 - 26\beta^2 + 27)(a_f^2 + v_f^2))}{3M_W^4 (s - M_Z^2)^2 \sin^4 \theta_W} \\
& - \frac{8\beta^2 E_e^4 e^4 v_f (3\beta^4 - 26\beta^2 + (3\beta^4 - 2\beta^2 + 3)\eta_T \xi_T \cos(2\phi - \phi_e + \phi_p) + 27)}{3M_W^4 (s - M_Z^2) \sin^2 \theta_W} \\
& + \frac{e^4 \eta_T \xi_T (3(\beta^2 - 1)^4 \log(\frac{1+\beta}{1-\beta})^2 - 4\beta(3\beta^6 + \beta^4 + \beta^2 + 3)) \cos(2\phi - \phi_e + \phi_p)}{24\beta M_W^4 \sin^2 \theta_W} \\
& - \frac{e^4 (3\beta^5 - \beta^3 + 3(\beta^2 - 1)^2 (\beta^2 + 1) \tanh^{-1}(\beta) - 3\beta)}{3\beta M_W^4 \sin^4 \theta_W} - \frac{e^4 (4\beta(3\beta^6 - 23\beta^4 + \beta^2 + 27))}{24\beta M_W^4} \\
& - \frac{e^4 (3(\beta^2 - 9)(\beta^2 - 1)^3 \log((\beta - 1)^2) - 6(\beta^2 - 9)(\beta^2 - 1)^3 \log(\beta + 1))}{24\beta M_W^4} \\
& - \frac{E_e^2 e^4 (a_f + v_f)(3(\beta^2 - 9)(\beta^2 - 1)^3 \log(\frac{1+\beta}{1-\beta})^2)}{12\beta M_W^4 (s - M_Z^2)} \\
& - \frac{E_e^2 \eta_T e^4 \xi_T (a_f - v_f)(4(3\beta^6 + \beta^4 + \beta^2 + 3)) \cos(2\phi - \phi_{e^-} + \phi_{e^+})}{12M_W^4 (s - M_Z^2) \sin^4 \theta_W} \\
& \left. - \frac{8\beta^2 E_e^4 e^4 ((3\beta^4 - 2\beta^2 + 3)\eta_T \xi_T (a_f^2 - v_f^2) \cos(2\phi - \phi_{e^-} + \phi_{e^+}))}{3M_W^4 (s - M_Z^2)^2 \sin^4 \theta_W} \right). \tag{B17}
\end{aligned}$$

After putting the values of masses, couplings, and energy of the beam in the nonoscillatory part of the above equation, while keeping the coefficient of the oscillatory part as a function of η_T , ξ_T , and $f(\beta_W)$, we find the following expression for the differential cross section:

$$\frac{d\sigma}{d\phi} = 427.968 + \eta_T \xi_T f(\beta) \cos(2\phi - \phi_{e^-} + \phi_{e^+}), \tag{B18}$$

where

$$\begin{aligned}
 f(\beta) = & \frac{(0.0261478\beta^8 - 0.104591\beta^6 + 0.156887\beta^4 - 0.104591\beta^2 + 0.0261478) \log((1 - \beta)^2)}{M_W^4} \\
 & - \frac{(0.0522956\beta^8 - 0.209182\beta^6 + 0.313774\beta^4 - 0.209182\beta^2 + 0.0522956) \log(1 + \beta)}{M_W^4} \\
 & - \frac{0.105566\beta^7 - 0.174968\beta^5 + 0.175293\beta^3 - 0.104591\beta}{M_W^4}.
 \end{aligned} \tag{B19}$$

2. IDM: $e^-(p_1, s_1)e^+(p_2, s_2) \rightarrow H^-(k_2)H^+(k_1)$

The amplitudes, in this case, for the s -channel diagrams containing a photon and Z boson, are given below as

$$\mathcal{M}_\gamma(s_1, s_2) = -\frac{ie^2}{s} \bar{u}(s_2, p_2) \gamma^\mu u(s_1, p_1) (k_1 - k_2)_\mu, \tag{B20}$$

$$\mathcal{M}_Z(s_1, s_2) = \frac{ig_Z(g_2 \cos \theta_W - g_1 \sin \theta_W)}{4(s - M_Z^2)} \bar{u}(s_2, p_2) \gamma^\mu (v_f - a_f \gamma_5) u(s_1, p_1) (k_1 - k_2)_\mu. \tag{B21}$$

The square amplitude for the process is given by

$$|\mathcal{M}|^2 = \sum_{s_i} \mathcal{M}(s_1, s_2) \mathcal{P}_{e^-}(s_1, s_3) \mathcal{P}_{e^+}(s_2, s_4) \mathcal{M}^\dagger(s_3, s_4), \tag{B22}$$

where

$$\mathcal{M} = \mathcal{M}_\gamma + \mathcal{M}_Z. \tag{B23}$$

The expressions for square amplitudes of the two diagrams along with their interference are written as

$$|\mathcal{M}|^2 = |\mathcal{M}_\gamma|^2 + |\mathcal{M}_Z|^2 + 2\text{Re}(\mathcal{M}_\gamma \mathcal{M}_Z^\dagger). \tag{B24}$$

Here,

$$|\mathcal{M}_\gamma|^2 = \frac{1}{4} \beta^2 s \theta^2 e^4 e^{-i(\phi_{e^-} + \phi_{e^+})} (2e^{i(\phi_{e^-} + \phi_{e^+})} - i\eta_T \xi_T \sin(2\phi) (e^{2i\phi_{e^-}} - e^{2i\phi_{e^+}}) + \eta_T \xi_T \cos(2\phi) (e^{2i\phi_{e^-}} + e^{2i\phi_{e^+}})), \tag{B25}$$

$$\begin{aligned}
 |\mathcal{M}_Z|^2 = & \frac{1}{(s - M_Z^2)^2 \tan^2 2\theta_W} [\beta^2 s \theta^2 E_e^4 g_Z^2 e^{-i(\phi_{e^-} + \phi_{e^+})} e^2 (2(a_f^2 + v_f^2) e^{i(\phi_{e^-} + \phi_{e^+})} \\
 & - \beta^2 (s \theta^2) E_e^4 g_Z^2 e^{-i(\phi_{e^-} + \phi_{e^+})} e^2 (\eta_T \xi_T (a_f^2 - v_f^2) \cos(2\phi) (e^{2i\phi_{e^-}} + e^{2i\phi_{e^+}})) \\
 & + i\beta^2 s \theta^2 E_e^4 g_Z^2 e^{-i(\phi_{e^-} + \phi_{e^+})} e^2 (\eta_T \xi_T (a_f^2 - v_f^2) \sin(2\phi) (e^{2i\phi_{e^-}} - e^{2i\phi_{e^+}}))],
 \end{aligned} \tag{B26}$$

$$\begin{aligned}
 \text{Re}(\mathcal{M}_\gamma \mathcal{M}_Z^\dagger) = & \frac{1}{2(s - M_Z^2) \tan 2\theta_W} [\beta^2 (c\theta^2 - 1) E_e^2 e^3 g_Z v_f e^{-i(\phi_{e^-} + \phi_{e^+})} (2e^{i(\phi_{e^-} + \phi_{e^+})} \\
 & + \beta^2 (s \theta^2) E_e^2 e^3 g_Z v_f e^{-i(\phi_{e^-} + \phi_{e^+})} (i\eta_T \xi_T \sin(2\phi) (e^{2i\phi_{e^-}} - e^{2i\phi_{e^+}}) \\
 & + \beta^2 (s \theta^2) E_e^2 e^3 g_Z v_f e^{-i(\phi_{e^-} + \phi_{e^+})} (\eta_T \xi_T \cos(2\phi) (e^{2i\phi_{e^-}} + e^{2i\phi_{e^+}}))].
 \end{aligned} \tag{B27}$$

In this case, the β is the boost for the H^\pm . From the above square amplitude, we obtain the differential cross section, after integrating over the variable θ , as

$$\frac{d\sigma}{d\phi} = \frac{3.894 \times 10^{11}}{64\pi^2 s} \left(\frac{8\beta^3 E_e^4 g_z^2 e^2 (a_f^2 - \eta_T \xi_T (a_f - v_f)(a_f + v_f) \cos(2\phi - \phi_{e^-} + \phi_{e^+}) + v_f^2)}{3(s - M_Z^2)^2 \tan^2 2\theta_W} + \frac{2}{3} \beta^3 e^4 (\eta_T \xi_T \cos(2\phi - \phi_{e^-} + \phi_{e^+}) + 1) - \frac{8\beta^3 E_e^2 e^3 g_z v_f (\eta_T \xi_T \cos(2\phi - \phi_{e^-} + \phi_{e^+}) + 1)}{3(s - M_Z^2) \tan 2\theta_W} \right). \quad (\text{B28})$$

With the values of masses, couplings, and energy of the beam, we find the differential cross section to be a function of η_T , ξ_T , and $f(\beta)$ as follows:

$$\frac{d\sigma}{d\phi} = 4.64277\beta^3 + 3.42967\eta_T \xi_T \beta^3 \cos(2\phi - \phi_{e^-} + \phi_{e^+}). \quad (\text{B29})$$

3. MSSM: $e^-(\mathbf{p}_1, s_1)e^+(\mathbf{p}_2, s_2) \rightarrow \chi^-(\mathbf{k}_1, s_3)\chi^+(\mathbf{k}_2, s_4)$

The amplitudes of two s -channel processes have the following expressions:

$$\mathcal{M}_\gamma(s_1, s_2, \lambda_3, \lambda_4) = \frac{ie^2}{s} \bar{v}(s_2, p_2) \gamma_\mu u(s_1, p_1) \bar{u}_\chi(\lambda_3, k_1) \gamma^\mu v_\chi(\lambda_4, k_2), \quad (\text{B30})$$

$$\mathcal{M}_Z(s_1, s_2, \lambda_3, \lambda_4) = \frac{ig_Z^2}{4(s - M_Z^2)} \bar{v}(s_2, p_2) \gamma^\mu (v_f - a_f \gamma_5) u(s_1, p_1) \bar{u}_\chi(\lambda_3, k_1) \gamma_\mu (v_\chi - a_\chi \gamma_5) v_\chi(\lambda_4, k_2). \quad (\text{B31})$$

The square of the amplitude is written as

$$|\mathcal{M}|^2 = \sum_{s_i, \lambda_j} \mathcal{M}(s_1, s_2, \lambda_3, \lambda_4) \mathcal{P}_{e^-(s_1, s_3)} \mathcal{P}_{e^+(s_2, s_4)} \mathcal{M}^\dagger(s_3, s_4, \lambda_3, \lambda_4), \quad (\text{B32})$$

where

$$\mathcal{M} = \mathcal{M}_\gamma + \mathcal{M}_Z. \quad (\text{B33})$$

The expressions for the square amplitude of two s -channel diagrams and their cross term are given as

$$|\mathcal{M}|^2 = |\mathcal{M}_\gamma|^2 + |\mathcal{M}_Z|^2 + 2\text{Re}(\mathcal{M}_\gamma \mathcal{M}_Z^\dagger). \quad (\text{B34})$$

Here,

$$|\mathcal{M}_\gamma|^2 = \frac{e^4}{2} (e^{-i(2\phi + \phi_{e^-} + \phi_{e^+})} \beta^2 (c\theta^2 - 1) \eta_T \xi_T (e^{2i(2\phi + \phi_{e^+})} + e^{2i\phi_{e^-}}) - (2(\beta^2 s\theta^2 - 2))), \quad (\text{B35})$$

$$\begin{aligned} |\mathcal{M}_Z|^2 = & \frac{1}{(s - M_Z^2)^2} [E_e^4 g_z^2 v_f^2 (a_\chi^2 \beta^2 (c\theta^2 + 1) + v_\chi^2 (\beta^2 (c\theta^2 - 1) + 2)) \\ & + E_e^4 g_z^2 (2a_f^2 (a_\chi^2 \beta^2 (c\theta^2 + 1) + v_\chi^2 (\beta^2 (c\theta^2 - 1) + 2)) + 16a_f a_\chi \beta c\theta v_f v_\chi) \\ & + (a_f^2 - v_f^2) E_e^4 g_z^2 e^{-i(2\phi + \phi_{e^-} + \phi_{e^+})} \beta^2 (s\theta^2) \eta_T \xi_T (a_\chi^2 + v_\chi^2) (e^{2i(2\phi + \phi_{e^+})} + e^{2i\phi_{e^-}})], \end{aligned} \quad (\text{B36})$$

$$\begin{aligned} \text{Re}(\mathcal{M}_\gamma \mathcal{M}_Z^\dagger) = & \frac{1}{2(s - M_Z^2)} [2E_e^2 e^2 g_z \beta^2 (c\theta^2 - 1) \eta_T \xi_T v_f v_\chi e^{2i\phi_{e^-}} + 2E_e^2 e^2 g_z (2a_f a_\chi \beta c\theta + v_f v_\chi (\beta^2 (c\theta^2 - 1) + 2)) \\ & + E_e^2 e^2 g_z e^{-i(2\phi + \phi_{e^-} + \phi_{e^+})} (\beta^2 (c\theta^2 - 1) \eta_T \xi_T v_f v_\chi e^{2i(2\phi + \phi_{e^+})})]. \end{aligned} \quad (\text{B37})$$

Here, the β stands for the boost of χ^\pm . Using the above matrix amplitude square, the differential cross section is found to be

$$\begin{aligned}
 \frac{d\sigma}{d\phi} = & \frac{3.894 \times 10^{11} \beta}{64\pi^2 s} \left(\frac{8E_e^2 e^2 g_z v_f v_\chi (\beta^2 \eta_T \xi_T \cos(2\phi - \phi_{e^-} + \phi_{e^+}) + \beta^2 - 3)}{3(s - M_Z^2)} \right. \\
 & + \frac{4E_e^4 g_z^2 (\beta^2 \eta_T \xi_T (a_f^2 - v_f^2)(a_f + v_f)(a_\chi^2 + v_\chi^2) \cos(2\phi - \phi_{e^-} + \phi_{e^+}))}{3(s - M_Z^2)^2} \\
 & \left. - \frac{4}{3} e^4 (\beta^2 \eta_T \xi_T \cos(2\phi - \phi_{e^-} + \phi_{e^+}) + \beta^2 - 3) + \frac{4E_e^4 g_z^2 ((a_f^2 + v_f^2)((3 - \beta^2)v_\chi^2 + 2a_\chi^2 \beta^2))}{3(s - M_Z^2)^2} \right). \quad (\text{B38})
 \end{aligned}$$

Substituting the values of all the couplings, masses, and beam energy except the m_χ , we obtain the expression for the differential cross section as

$$\frac{d\sigma}{d\phi} = 52.4371\beta - 17.457\beta^3 - 0.966784\beta^3 \eta_T \xi_T \cos(2\phi + \phi_{e^+} - \phi_{e^-}). \quad (\text{B39})$$

-
- [1] G. Apollinari, O. Brüning, T. Nakamoto, and L. Rossi, High Luminosity Large Hadron Collider HL-LHC, CERN Yellow Report No. 5 (2015), pp. 1–19 [arXiv:1705.08830].
- [2] P. Azzi *et al.*, Report from working group 1: Standard model physics at the HL-LHC and HE-LHC, CERN Yellow Rep. Monogr. **7**, 1 (2019).
- [3] G. Aarons *et al.* (ILC Collaboration), International linear collider reference design report volume 2: Physics at the ILC, arXiv:0709.1893.
- [4] H. Baer, T. Barklow, K. Fujii, Y. Gao, A. Hoang, S. Kanemura, J. List, H. E. Logan, A. Nomerotski, M. Perelstein *et al.*, The international linear collider technical design report—volume 2: Physics, arXiv:1306.6352.
- [5] T. Behnke, J. E. Brau, B. Foster, J. Fuster, M. Harrison, J. M. Paterson, M. Peskin, M. Stanitzki, N. Walker, and H. Yamamoto, The international linear collider technical design report—volume 1: Executive summary, arXiv:1306.6327.
- [6] P. Bambade *et al.*, The international linear collider: A global project, arXiv:1903.01629.
- [7] P. Agostini *et al.* (LHeC and FCC-he Study Group Collaborations), The large hadron-electron collider at the HL-LHC, J. Phys. G **48**, 110501 (2021).
- [8] A. Abada *et al.* (FCC Collaboration), FCC-ee: The lepton collider: Future circular collider conceptual design report volume 2, Eur. Phys. J. Spec. Top. **228**, 261 (2019).
- [9] A. Abada *et al.* (FCC Collaboration), FCC-hh: The hadron collider: Future circular collider conceptual design report volume 3, Eur. Phys. J. Spec. Top. **228**, 755 (2019).
- [10] M. Asano, T. Saito, T. Suehara, K. Fujii, R. S. Hundi, H. Itoh, S. Matsumoto, N. Okada, Y. Takubo, and H. Yamamoto, Discrimination of new physics models with the international linear collider, Phys. Rev. D **84**, 115003 (2011).
- [11] I. F. Ginzburg, Measuring mass and spin of Dark Matter particles with the aid energy spectra of single lepton and dijet at the e^+e^- linear collider, J. Mod. Phys. **5**, 1036 (2014).
- [12] A. Belyaev, A. Freegard, I. F. Ginzburg, D. Locke, and A. Pukhov, Decoding Dark Matter at future e^+e^- colliders, Phys. Rev. D **106**, 015016 (2022).
- [13] F. Boudjema and R. K. Singh, A model independent spin analysis of fundamental particles using azimuthal asymmetries, J. High Energy Phys. **07** (2009) 028.
- [14] N. D. Christensen and D. Salmon, New method for the spin determination of dark matter, Phys. Rev. D **90**, 014025 (2014).
- [15] A. Belyaev, L. Panizzi, A. Pukhov, and M. Thomas, Dark matter characterization at the LHC in the effective field theory approach, J. High Energy Phys. **04** (2017) 110.
- [16] G. Moortgat-Pick *et al.*, The role of polarized positrons and electrons in revealing fundamental interactions at the linear collider, Phys. Rep. **460**, 131 (2008).
- [17] N. G. Deshpande and E. Ma, Pattern of symmetry breaking with two Higgs doublets, Phys. Rev. D **18**, 2574 (1978).
- [18] D. Majumdar and A. Ghosal, Dark matter candidate in a heavy Higgs model—direct detection rates, Mod. Phys. Lett. A **23**, 2011 (2008).
- [19] H. E. Haber, Introductory low-energy supersymmetry, in Theoretical Advanced Study Institute (TASI 92): From Black Holes and Strings to Particles (1993), pp. 589–686, arXiv:hep-ph/9306207.
- [20] J. Wess and J. Bagger, *Supersymmetry and Supergravity* (Princeton University Press, Princeton, NJ, USA, 1992).
- [21] R. Barbieri, L. J. Hall, and V. S. Rychkov, Improved naturalness with a heavy Higgs: An Alternative road to LHC physics, Phys. Rev. D **74**, 015007 (2006).
- [22] M. Drees, R. Godbole, and P. Roy, Theory and Phenomenology of Sparticles: An Account of Four-Dimensional $N = 1$ Supersymmetry in High Energy Physics (World Scientific, Singapore, 2004).
- [23] S. Y. Choi, A. Djouadi, H. K. Dreiner, J. Kalinowski, and P. M. Zerwas, Chargino pair production in $e + e^-$ collisions, Eur. Phys. J. C **7**, 123 (1999).
- [24] A. Belyaev, G. Cacciapaglia, I. P. Ivanov, F. Rojas-Abatte, and M. Thomas, Anatomy of the inert two Higgs doublet

- model in the light of the LHC and non-LHC dark matter searches, *Phys. Rev. D* **97**, 035011 (2018).
- [25] J. Haller, A. Hoecker, R. Kogler, K. Mönig, T. Peiffer, and J. Stelzer, Update of the global electroweak fit and constraints on two-Higgs-doublet models, *Eur. Phys. J. C* **78**, 675 (2018).
- [26] A. Tumasyan *et al.* (CMS Collaboration), Search for invisible decays of the Higgs boson produced via vector boson fusion in proton-proton collisions at $\sqrt{s} = 13$ TeV, *Phys. Rev. D* **105**, 092007 (2022).
- [27] ATLAS Collaboration, Measurement of the properties of Higgs boson production at $\sqrt{s} = 13$ TeV in the $H \rightarrow \gamma\gamma$ channel using 139 fb⁻¹ of pp collision data with the ATLAS experiment, [arXiv:2207.00348](https://arxiv.org/abs/2207.00348).
- [28] W. Kilian, T. Ohl, and J. Reuter, WHIZARD: Simulating multi-particle processes at LHC and ILC, *Eur. Phys. J. C* **71**, 1742 (2011).
- [29] T. Sjöstrand, S. Ask, J. R. Christiansen, R. Corke, N. Desai, P. Ilten, S. Mrenna, S. Prestel, C. O. Rasmussen, and P. Z. Skands, An introduction to PYTHIA 8.2, *Comput. Phys. Commun.* **191**, 159 (2015).
- [30] J. de Favereau, C. Delaere, P. Demin, A. Giammanco, V. Lemaître, A. Mertens, and M. Selvaggi (DELPHES 3 Collaboration), DELPHES 3, A modular framework for fast simulation of a generic collider experiment, *J. High Energy Phys.* **02** (2014) 057.
- [31] D. R. Yennie, S. C. Frautschi, and H. Suura, The infrared divergence phenomena and high-energy processes, *Ann. Phys. (N.Y.)* **13**, 379 (1961).
- [32] B. Ananthanarayan and S. D. Rindani, Transverse beam polarization and CP violation in $e^+e^- \rightarrow \gamma Z$ with contact interactions, *Phys. Lett. B* **606**, 107 (2005).
- [33] C. P. Burgess and J. A. Robinson, Transverse polarization at e^+e^- colliders and CP violation from new physics, *Int. J. Mod. Phys. A* **06**, 2707 (1991).
- [34] T. G. Rizzo, Transverse polarization signatures of extra dimensions at linear colliders, *J. High Energy Phys.* **02** (2003) 008.
- [35] B. Ananthanarayan, S. D. Rindani, R. K. Singh, and A. Bartl, Transverse beam polarization and CP -violating triple-gauge-boson couplings in $e^+e^- \rightarrow \gamma Z$, *Phys. Lett. B* **593**, 95 (2004).
- [36] S. D. Rindani, Transverse beam polarization and limits on leptoquark couplings in $e^+e^- \rightarrow t\bar{t}$, *Phys. Lett. B* **602**, 97 (2004).
- [37] K.-i. Hikasa, Transverse polarization effects in e^+e^- collisions: The role of chiral symmetry, *Phys. Rev. D* **33**, 3203 (1986).
- [38] R. M. Godbole, S. K. Rai, and S. D. Rindani, Use of transverse polarization to probe R-parity violating supersymmetry at ILC, *Phys. Lett. B* **678**, 395 (2009).